Efficient Raw Signal Generation Based on Equivalent Scatterer and Subaperture Processing for SAR with Arbitrary Motion

Hongtu XIE, Daoxiang AN, Xiaotao HUANG, Zhimin ZHOU

College of Electronic Science and Engineering, National University of Defense Technology, Changsha, Hunan, P. R. China, 410073

xht20041623@163.com

Abstract. *An efficient SAR raw signal generation method based on equivalent scatterer and subaperture processing is proposed in this paper. It considers the radar's motion track, which can obtain the precise raw signal for the real SAR. First, the imaging geometry with arbitrary motion is established, and then the scene is divided into several equidistant rings. Based on the equivalent scatterer model, the approximate expression of the SAR system transfer function is derived, thus each pulse's raw signal can be generated by the convolution of the transmitted signal and system transfer function, performed by the fast Fourier transform (FFT). To further improve the simulation efficiency, the subaperture and polar subscene processing is used. The system transfer function of pulses for the same subaperture is calculated simultaneously by the weighted sum of all subscenes' equivalent backscattering coefficient in the same equidistant ring, performed by the nonuniform FFT (NUFFT). The method only involves the FFT, NUFFT and complex multiplication operations, which means the easier implementation and higher efficiency. Simulation results are given to prove the validity of this method.*

Keywords

Arbitrary motion, equivalent scatterer, raw signal generation, synthetic aperture radar, subaperture processing.

1. Introduction

Synthetic aperture radar (SAR) plays a significant role in the remote sensing, geosciences, and surveillance applications. It can effectively operate in severe weather condition and achieve high resolution images [1]-[3].

SAR raw signal generation technology is a key ring in the research and development of SAR system and takes an important role in many aspects, such as the system design, parameter optimization, meeting different requirements, testing of imaging algorithms, analyzing the jamming and noises, etc. [4]-[5]. To ensure that designed SAR systems satisfy the specific requirements of the different users, raw signal generation and imaging processing should be carried out before the development of the SAR systems. Therefore, the SAR raw signal generation is a significant component of the SAR simulation technology.

Generally, the SAR raw signal generation of discrete scattering targets is suitable for testing the performance of imaging algorithms and for testing system parameters such as the resolution, peak sidelobe ratio (PSLR), and integral sidelobe ratio, etc. When the number of targets is small, the raw signal can be calculated pulse by pulse and target by target (TBT) according to the SAR geometry. It works in the time domain and can generate precise raw signal [6]. However, as the jamming, thermal noise, clutter, multipath, analog-to-digital quantization errors and image ambiguity are concerned, the natural scene raw signal has to be generated. For the natural scene raw signal generation, there are some difficulties from two aspects. One is the simulation of the natural scene's backscattering coefficient, and the other is the efficient raw signal generation method while a large number of scatterers are contained. As to the former problem, the simulation of the natural scene's backscattering coefficient has been investigated by several researchers, which has been partially indicated in [7]-[14]. In this paper, we focus on the latter problem, which means that the natural scene's backscattering coefficient is known and considered as the input in the raw signal generation.

In general, the SAR raw signal generation algorithms include the TBT [15] method in the time domain, the one-dimensional fast Fourier transform (1D FFT) algorithm, the two-dimensional FFT (2D FFT) algorithm in frequency-domain and imaging inverse processing (IMIP) algorithm. TBT algorithm calculates the raw signal by adding all distributed point targets' echo coherently, according to the imaging geometry, so it works pulse by pulse and target by target. It doesn't make any approximation, thus it has the highest accuracy. However, it costs huge calculation and time, thus it is only suitable for small number of discrete scattering targets' raw signal generation. 2D FFT method is first proposed by Franceschetti [16]-[19]. He developed

a series of SAR raw signal simulators for terrain scenes, such as bare land ground, sea surface, and buildings, and then provided a series of improved versions. It was realized by multiplying the 2D spectrum of the targets' scattering characteristic and 2D frequency-domain expression of the SAR system transfer function, and the time domain raw signal is obtained using 2D inverse FFT (IFFT). Compared with the TBT algorithm, the simulation efficiency of 2D FFT algorithm is improved obviously. However, when the radar's motion errors exist, it is very difficult to simulate these errors for the SAR raw signal generation. Therefore, the 2D FFT algorithm is restricted by the radar's motion errors. IMIP [20]-[22] is to transform the image data into signal space by the inverse imaging processing, and then the simulated raw signal is obtained. Its efficiency is also higher than that of the TBT method. However, it is also limited by the radar's motion errors. When SAR system contains these errors, the simulated raw signal by the 2D FFT or IMIP methods is imprecise. 1D FFT algorithm [23]-[24] generates the SAR raw signal by the convolution of the radar signal and SAR system impulse response function, which is performed by the FFT. It also works pulse by pulse, so it is especially useful for the raw signal generation of the natural scene when the radar's motion errors exist. Its efficiency is higher than that of the TBT method, but lower than that of 2D FFT and IMIP methods.

To make a compromise between the simulation efficiency and precision, the reference [25] proposed a subaperture based echo simulation algorithm. It used the FFT to simultaneously calculate the SAR system transfer function for the same subaperture pulses, then subaperture pulses' raw signal is generated by the convolution of the transmitted signal and system transfer function using the FFT, which can further improve the simulation efficiency. But, it doesn't consider the radar's motion error, which can't obtain the precise raw signal of the nature scene for the real SAR system. Reference [26] presented a raw signal simulation algorithm based on subaperture processing. First, the FFT algorithm in range dimension is used to get the central pulse's echo signal of a sub-aperture. Then, the 1st-order approximate model of slant range in azimuth dimension is utilized to generate other pulses' echo signal in a sub-aperture. However, it also doesn't consider the radar's motion error in the simulation.

Based on these previous works, this paper explores an efficient SAR raw signal generation algorithm based on the equivalent scatterer and subaperture processing. It considers the radar's motion track to generate the high-precision raw signal. The subaperture processing and nonuniform FFT (NUFFT) are used to simultaneously calculate the SAR system transfer function for the same subaperture pulses, then subaperture pulses' raw signal is generated by the convolution of the transmitted signal and system transfer function using the FFT. The utilization of the equivalent scatterer, subaperture processing and FFT (NUFFT) operation can greatly improve the SAR raw signal simulation efficiency.

This paper is organized as follows. Section 2 presents the SAR geometry mode, and the raw signal generation based on equivalent scatterer is introduced. Section 3 gives a detail description of the proposed raw signal generation method. First, the SAR geometry mode in polar coordinate is established; and then the subaperture processing in this method is derived; finally implementation of the proposed method is discussed. The validity of the proposed approach is proved in Section 4 based on the simulation data. Section 5 provides the conclusion.

2. SAR Raw Signal Generation based on Equivalent Scatterer

2.1 Geometry Model

Because the radar speed is much less than the speed of light, the stop and go assumption is commonly used in SAR [1]. In other words, the radar's antenna is assumed to be at a standstill during ranging signal propagation and it moves on to the next position only after the echo signal is received. According to this hypothesis, the signal can be modeled as a function of two independent variables, i.e., the fast time and slow time. However, its validity needs to be evaluated in each particular SAR case. Here, we assumed that the stop and go assumption is valid for the SAR signal generation.

SAR geometry model with arbitrary motion is shown in Fig. 1. The dashed straight line parallel to the Y axis is the radar's nominal track, while the solid curve is its actual track. The radar coordinates are $(x(\eta), y(\eta), z(\eta))$ at the slow time η. The simulated scene is composed of large numbers of point targets distributed on the rectangle grid. Provided that the scene grid has dimensions $M \times N$, and range and azimuth intervals between the adjacent grids are Δx and Δy, respectively. $x_{\min}$ is the minimum ground range of the scene, and its azimuth centre line is the X axis. So the range between the radar and the grid (m,n) at η is

$$R(\eta,m,n) = [\left(x(\eta) - (x_{\min} + m \cdot \Delta x)\right)^2 + \left(y(\eta) - (n - N/2) \cdot \Delta y\right)^2 + \left(z(\eta)\right)^2]^{1/2} \quad (1)$$

where $1 \le m \le M$, $1 \le n \le N$

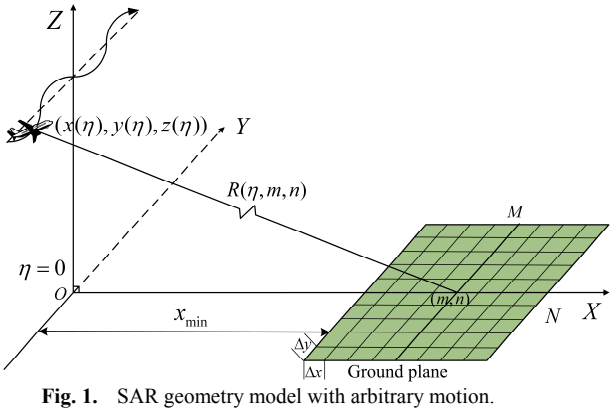

Fig. 1. SAR geometry model with arbitrary motion.

Suppose that the transmitted signal is a chirp signal

$$p(\tau) = w_r(\tau) \cdot \exp(j2\pi f_c \tau + j\pi\gamma\tau^2) \tag{2}$$

where τ is the fast time, γ is the chirp rate, $w_r(\cdot)$ is the range envelope and f_c is the center frequency. Because the scene can be separated into large numbers of point targets, the scene's raw signal can be represented as

$$\begin{aligned} s(\tau,\eta) = &\sum_{m=1}^{M}\sum_{n=1}^{N} \sigma_{mn} w_r\left[\tau - 2R(\eta,m,n)/c\right] \\ &\cdot \exp\left[-j4\pi f_c R(\eta,m,n)/c + j\pi\gamma\left(\tau - 2R(\eta,m,n)/c\right)^2\right] \end{aligned} \tag{3}$$

where σ_{mn} is target's backscattering coefficient of the grid (m,n), and c is the speed of light.

2.2 Calculate Equivalent Scatterer's Backscattering Coefficients

From (3), we can find that it is easy to generate the raw signal in time domain, but it has high computational load. To improve the simulation efficiency, this paper first introduces a fast raw signal generation method based on the equivalent scatterer. Its basic idea is to divide the scene into several equidistant rings, and targets on rectangle grids can be considered as distributing in those equidistant rings that nominally exist, which is shown in Fig. 2. Therefore, backscattering coefficient of targets in the same equidistant ring can be substituted for an equivalent scatterer.

Assume that Δs is the interval between the adjacent equidistant rings. $R_{\min}(\eta)$ and $R_{\max}(\eta)$ are the minimum and maximum ranges from the radar to the scene at η, respectively. Then, the number of equidistant rings is

$$N_p(\eta) = round\left((R_{\max}(\eta) - R_{\min}(\eta))/\Delta s\right) + 1 . \tag{4}$$

Then, the range of grid (*m, n*) meets the following inequality

$$R_{\min}(\eta) + (p-1)\Delta s \le R(\eta,m,n) \le R_{\min}(\eta) + p\Delta s \quad 1 \le p \le N_p(\eta) . \tag{5}$$

Targets' distribution between two adjacent equidistant rings is shown in Fig. 3. *p*-1 and *p* denote two adjacent equidistant rings, and the ranges from them to the radar are $R_{\min}(\eta) + (p-1)\Delta s$ and $R_{\min}(\eta) + p\Delta s$, respectively.

The spacing between the (*p*-1)-th and *p*-th equidistant rings is defined as the *p*-th equidistant ring domain. The dashed ring is the center of the equidistant ring domain, and the range from it to the radar is

$$R(\eta,p) = R_{\min}(\eta) + (p - 1/2)\Delta s . \tag{6}$$

To calculate the targets' backscattering coefficients in the equidistant ring domain's center, the range between the radar and the targets in the equidistant ring domain is approximately replaced by the range from the radar to the equidistant ring domain's center. Therefore, the equivalent scatterer is substituted for all targets in this domain, whose backscattering coefficient is computed by

$$\sigma(\eta,p) = \sum_{i=1}^{I_p} \sigma_i \exp\left[-j4\pi f_c \Delta R_i(\eta,p)/c\right] \tag{7}$$

where I_p is the number of targets in the *p*-th equidistant ring domain, σ_i is the backscattering coefficient of the *i*-th target in this domain. $\Delta R_i(\eta,p)$ is the difference between the range from the *i*-th target to the radar (i.e., $R_i(\eta)$) and the range from the *p*-th equidistant ring domain's center to the radar, which can be given by

$$\Delta R_i(\eta,p) = R_i(\eta) - \left(R_{\min}(\eta) + (p - 1/2)\Delta s\right) . \tag{8}$$

So the raw signal of the scene can be also expressed as

$$\begin{aligned} s(\tau,\eta) = &\sum_{p=1}^{N_p(\eta)} \sigma(\eta,p) \exp\left[-j4\pi f_c R(\eta,p)/c\right] \\ &\cdot w_r\left[\tau - 2R(\eta,p)/c\right] \exp\left[j\pi\gamma\left(\tau - 2R(\eta,p)/c\right)^2\right] \end{aligned} \tag{9}$$

We can find that the latter two items of (9) are only related to the fast time τ. So the raw signal of the scene can also be written in the following convolution format

$$\begin{aligned} s(\tau,\eta) = &w_r(\tau)\exp(j\pi\gamma\tau^2) \otimes_\tau \sum_{p=1}^{N_p} \sigma(\eta,p) \\ &\cdot \exp\left[-j4\pi f_c R(\eta,p)/c\right] \cdot \delta\left[\tau - 2R(\eta,p)/c\right] \end{aligned} \tag{10}$$

where $\otimes_\tau$ is the convolution versus the fast time τ. The physical meanings of (10) is that the received signal of the radar is the response of a linear time-invariant system, the system's input is the transmitted base-band chirp signal, and its output is the result of the convolution between the transmitted signal and the impulse response function with a certain amplitude, phase and delay.

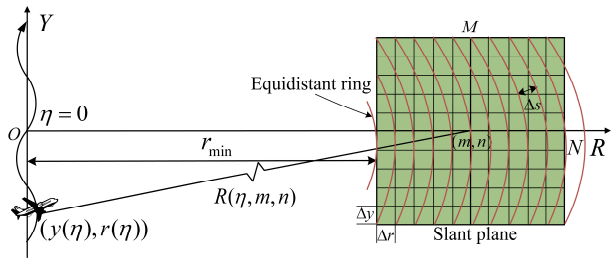

Fig. 2. Geometry model in slant plane.

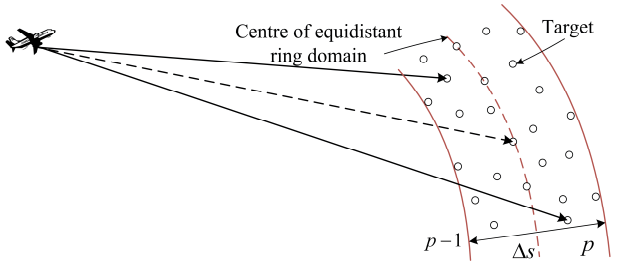

Fig. 3. Targets' distribution between adjacent equidistant rings

It is known that the convolution can be performed by the FFT, so the raw signal of the scene is given by

$$s(\tau,\eta)=\mathrm{IFFT}\left\{\mathrm{FFT}\left[w_r(\tau)\exp(j\pi\gamma\tau^2)\right]\cdot\mathrm{FFT}\left[\sum_{p=1}^{N_p}\sigma(\eta,p)\exp\left(-j4\pi f_c R(\eta,p)/c\right)\cdot\delta\left(\tau-2R(\eta,p)/c\right)\right]\right\} \tag{11}$$

3. SAR Raw Signal Generation Based on Subaperture Processing

SAR raw signal generation method in Section 2 can improve the simulation efficiency to a certain extent. Since the raw signal is calculated pulse by pulse and equivalent scatterer by equivalent scatterer, thus generation with the large number of pulses is not suitable for the raw signal.

In order to further improve the simulation efficiency, the subaperture and polar subscene processing is used. Based on the above method, the system transfer function of pulses for the same subaperture can be calculated by the weighted sum of all subscenes' equivalent backscattering coefficient in the same equidistant ring.

3.1 Geometry Model in Polar Coordinate

SAR geometry model in polar coordinate is shown in Fig. 4. Assume that A_c is the synthetic aperture center at aperture center time η_c, A_η is the aperture position at η. Let ρ be the range between A_c and the scene and θ be the angle between ρ and the Y positive axis, respectively. $\Delta\theta$ is the angular sampling spacing of the scene. (p,k) is the k-th polar subscene in the p-th equidistant ring domain, and $R(\eta,p,k)$ is the range between it and A_η at η. Targets in the scene can be considered as distributing in a large number of small subscenes depicted as red arc and dashed line in Fig. 4. So, the scene's raw signal can be rewritten as

$$s(\tau,\eta)=w_r(\tau)\exp(j\pi\gamma\tau^2)\otimes_\tau\sum_{p=1}^{N_p(\eta)}\sum_{k=1}^{N_k(\eta)}\sigma(\eta,\rho_p,\theta_k)\cdot\exp\left[-j4\pi f_c R(\eta,\rho_p,\theta_k)/c\right]\cdot\delta\left[\tau-2R(\eta,\rho_p,\theta_k)/c\right] \tag{12}$$

where $N_k(\eta)$ is the number of the polar subscenes at η. $R(\eta,\rho_p,\theta_k)$ is the range from the radar to the k-th subscene in the p-th equidistant ring domain. $\sigma(\eta,\rho_p,\theta_k)$ stands for the backscattering coefficient of this equivalent scatterer (polar subscene), which can be computed as

$$\sigma(\eta,\rho_p,\theta_k)=\sum_{i=1}^{I_{p,k}}\sigma_i\exp\left[-j4\pi f_c\left(R_i(\eta)-R(\eta,\rho_p,\theta_k)\right)/c\right]. \tag{13}$$

where $I_{p,k}$ is the number of targets in the k-th subscene of the p-th equidistant ring domain.

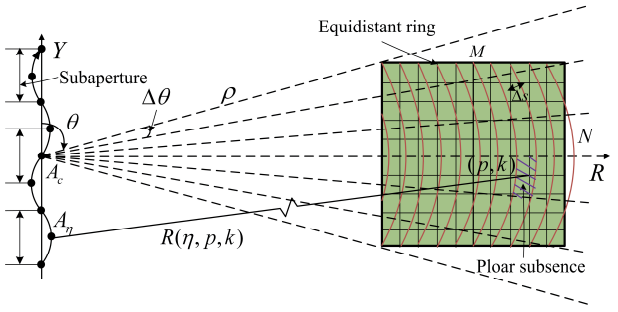

Fig. 4. Geometry model in polar coordinate.

3.2 Subaperture Processing

In the following, SAR raw signal generation method based subaperture processing is derived in detail.

Radar pulses are split into several small subapertures (see Fig. 4). Each subaperture contains the same number of radar pulses. We assume that each subaperture time is very short, thus all pulses in the same subaperture can be considered as sharing the same scene scope. The SAR raw signal generation based on the subaperture processing is shown in Fig. 5. Taking the n-th subaperture for example, $A_{\eta_{nc}}$ is the center pulse position, A_{η_n} is the radar's current position. ρ_n and θ_n are the corresponding scene polar coordinates, and $\Delta\theta_n$ is the corresponding scene angular sampling spacing. d_{η_n} is the length of the straight line $\overline{A_{\eta_{nc}}A_{\eta_n}}$, and β_{η_n} is the angle between $\overline{A_{\eta_{nc}}A_{\eta_n}}$ and the Y axis. $T(\rho_p,\theta_{n0})$ and $T'(\rho_p,\theta_{n0}+k\Delta\theta_n)$ are two polar subscenes in the p-th equidistant ring domain.

Taking into account the central pulse position $A_{\eta_{nc}}$ of the n-th subaperture, $R(\eta,\rho_p,\theta_k)$ in (12) is the same to each polar subscene in the p-th equidistant ring domain. Thus, (12) can be written as

$$s(\tau,\eta_{nc})=w_r(\tau)\exp(j\pi\gamma\tau^2)\otimes_\tau\sum_{p=1}^{N_p(\eta_{nc})}\sum_{k=-N_k(\eta_{nc})/2}^{N_k(\eta_{nc})/2}\sigma(\eta_{nc},\rho_{np},\theta_{nk})\cdot\exp\left[-j4\pi f_c R(\eta_{nc},\rho_{np})/c\right]\cdot\delta\left[\tau-2R(\eta_{nc},\rho_{np})/c\right] \tag{14}$$

where $R(\eta_{nc},\rho_{np})$ denotes the range from the central pulse position $A_{\eta_{nc}}$ to the p-th equidistant ring domain.

As taking into account other pulse position A_{η_n} rather than the central pulse position $A_{\eta_{nc}}$, the range $R(\eta_n,\rho_{np},\theta_{nk})$ is different from the range $R(\eta_{nc},\rho_{np})$. However, the range

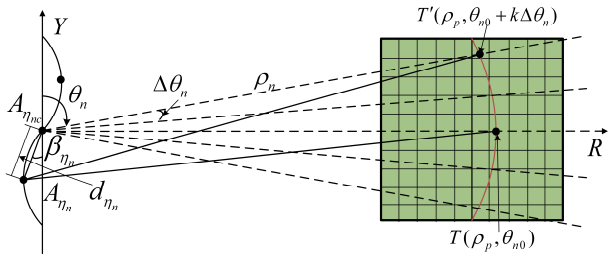

Fig. 5. Subaperture processing.

$R(\eta_n,\rho_{np},\theta_{nk})$ can be computed from the range $R(\eta_{nc},\rho_{np})$ according to the subaperture geometry model in Fig. 5.

Then, we can get the following relationship

$$\begin{aligned} R(\eta_n,\rho_{np},\theta_{nk}) &= \left|A_{n\eta}T'\right| \\ &= \left|A_{nc}T'\right| + \left(\left|A_{n\eta}T'\right| - \left|A_{nc}T'\right|\right) \\ &= \left|A_{nc}T'\right| + \left(\left|A_{n\eta}T'\right| - \left|A_{n\eta}T\right|\right) + \left(\left|A_{n\eta}T\right| - \left|A_{nc}T'\right|\right) \\ &= \left|A_{nc}T'\right| + \left(\left|A_{n\eta}T'\right| - \left|A_{n\eta}T\right|\right) + \left(\left|A_{n\eta}T\right| - \left|A_{nc}T\right|\right) \\ &= R(\eta_{nc},\rho_{np}) + \Delta R_1 + \Delta R_2 \end{aligned} \tag{15}$$

From (15), it is found that both $R(\eta_{nc},\rho_{np})$ and ΔR_2 are independent of the variable *k*. Thus, (12) can be written as

$$\begin{aligned} s(\tau,\eta_n) = w_r(\tau)\exp(j\pi\gamma\tau^2) \otimes_\tau & \sum_{p=1}^{N_p(\eta_{nc})} \sum_{k=-N_k(\eta_{nc})/2}^{N_k(\eta_{nc})/2} \sigma(\eta_n,\rho_{np},\theta_{nk}) \\ & \cdot \exp\left[-j4\pi f_c\left(R(\eta_{nc},\rho_{np}) + \Delta R_1 + \Delta R_2\right)/c\right] \\ & \cdot \delta\left[\tau - 2R(\eta_n,\rho_{np},\theta_{nk})/c\right] \end{aligned} \tag{16}$$

Provided that each subaperture time is very short, it is reasonable that the backscattering coefficient $\sigma(\eta_n,\rho_{np},\theta_{nk})$ is approximately substituted by $\sigma(\eta_{nc},\rho_{np},\theta_{nk})$. We further assume that radar's beamwidth is not very wide, so $R(\eta_n,\rho_{np},\theta_{nk})$ is also approximated as $R(\eta_n,\rho_{np},\theta_{n0})$, which hardly impacts the value of $\delta\left[\tau - 2R(\eta_n,\rho_{np},\theta_{nk})/c\right]$ in the digital signal processing. Thus, (16) is approximated as

$$\begin{aligned} s(\tau,\eta_n) \approx w_r(\tau)\exp(j\pi\gamma\tau^2) \otimes_\tau & \sum_{p=1}^{N_p(\eta_{nc})} \left\{\delta\left[\tau - 2R(\eta_n,\rho_{np},\theta_{n0})/c\right]\right. \\ & \left[\sum_{k=-N_k(\eta_{nc})/2}^{N_k(\eta_{nc})/2} \sigma(\eta_{nc},\rho_{np},\theta_{nk}) \cdot \exp\left[-j4\pi f_c \Delta R_1/c\right]\right] \\ & \left. \cdot \exp\left[-j4\pi f_c\left(R(\eta_{nc},\rho_{np}) + \Delta R_2\right)/c\right]\right\} \end{aligned} \tag{17}$$

Here, we define the backscattering coefficient of the *p*-th equidistant ring domain at the pulse position A_{η_n} as

$$\sigma(\eta_n,\rho_{np}) = \sum_{k=-N_k(\eta_{nc})/2}^{N_k(\eta_{nc})/2} \sigma(\eta_{nc},\rho_{np},\theta_{nk}) \cdot \exp\left[-j4\pi f_c \Delta R_1/c\right]. \tag{18}$$

We use R_p to denote the range $R(\eta_{nc},\rho_{np})$, then we have

$$\begin{aligned} \left|A_{n\eta}T\right| &= \sqrt{R_p^2 + d_{\eta_n}^2 + 2R_p d_{\eta_n}\cos(\theta_{n0} - \beta_{\eta_n})} \\ &= R_p\sqrt{1 + d_{\eta_n}^2/R_p^2 + 2d_{\eta_n}\cos(\theta_{n0} - \beta_{\eta_n})/R_p} \end{aligned} \tag{19}$$

It is known that (19) can be expanded by the Taylor series

$$\begin{aligned} \left|A_{n\eta}T\right| &= R_p\left[1 + \frac{1}{2}\left(d_{\eta_n}^2/R_p^2 + 2d_{\eta_n}\cos(\theta_{n0} - \beta_{\eta_n})/R_p\right)\right. \\ &\quad \left. -\frac{1}{8}\left(d_{\eta_n}^2/R_p^2 + 2d_{\eta_n}\cos(\theta_{n0} - \beta_{\eta_n})/R_p\right)^2 + \cdots\right] \\ &= R_p + d_{\eta_n}\cos(\theta_{n0} - \beta_{\eta_n}) + \frac{d_{\eta_n}^2}{2R_p}\sin^2(\theta_{n0} - \beta_{\eta_n}) + \cdots \end{aligned} \tag{20}$$

Due to the fact that $d_{\eta_n} << R_p$, terms excepted the first two terms of (20) are approximated to zeros. Only considering the first two terms of (20), $\left|A_{n\eta}T\right|$ is approximated as

$$\left|A_{n\eta}T\right| \approx R_p + d_{\eta_n}\cos(\theta_{n0} - \beta_{\eta_n}) \ . \tag{21}$$

In a similar way, the range $\left|A_{n\eta}T'\right|$ is given by

$$\left|A_{n\eta}T'\right| = R_p\sqrt{1 + d_{\eta_n}^2/R_p^2 + 2d_{\eta_n}\cos(\theta_{n0} + k\Delta\theta_n - \beta_{\eta_n})/R_p} \tag{22}$$

and then approximated as

$$\left|A_{n\eta}T'\right| \approx R_p + d_{\eta_n}\cos(\theta_{n0} + k\Delta\theta_n - \beta_{\eta_n}) \ . \tag{23}$$

Then the range difference between $\left|A_{n\eta}T\right|$ and $\left|A_{n\eta}T'\right|$ is

$$\begin{aligned} \Delta R_1 &= \left|A_{n\eta}T'\right| - \left|A_{n\eta}T\right| \\ &\approx d_{\eta_n}\left(\cos(\theta_{n0} + k\Delta\theta_n - \beta_{\eta_n}) - \cos(\theta_{n0} - \beta_{\eta_n})\right) \end{aligned} \tag{24}$$

Under the above assumption that radar's beamwidth is not very wide, then the value $k\Delta\theta_n$ is usually small enough. So $\cos(\theta_{n0} + k\Delta\theta_n - \beta_{\eta_n}) - \cos(\theta_{n0} - \beta_{\eta_n}) \approx -k\Delta\theta_n\sin(\theta_{n0} - \beta_{\eta_n})$ is reasonable. Then the range difference ΔR_1 becomes

$$\Delta R_1 \approx -d_{\eta_n}k\Delta\theta_n\sin(\theta_{n0} - \beta_{\eta_n}) \ . \tag{25}$$

Then, (18) can be written as

$$\begin{aligned} \sigma(\eta_n,\rho_{np}) = & \sum_{k=-N_k(\eta_{nc})/2}^{N_k(\eta_{nc})/2} \sigma(\eta_{nc},\rho_{np},\theta_{nk}) \\ & \cdot \exp\left[j4\pi f_c d_{\eta_n}k\Delta\theta_n\sin(\theta_{n0} - \beta_{\eta_n})/c\right] \end{aligned} \tag{26}$$

If the angular sampling spacing of the scene for the *n*-th subaperture satisfies the following relationship

$$\Delta\theta_n = c/\left(2f_c d_{T_n}\right). \tag{27}$$

where d_{T_n} is the range from the center pulse position $A_{\eta_{nc}}$ to the edge pulse position in the *n*-th subaperture, then (27) can be written as

$$\begin{aligned} \sigma(\eta_n,\rho_{np}) = & \sum_{k=-N_k(\eta_{nc})/2}^{N_k(\eta_{nc})/2} \sigma(\eta_{nc},\rho_{np},\theta_{nk}) \\ & \cdot \exp\left[j2\pi k d_{\eta_n}\sin(\theta_{n0} - \beta_{\eta_n})/d_{T_n}\right] \end{aligned} \tag{28}$$

Assume that the size of the *n*-th subaperture is L_n, and its index is $l_n = -L_n/2 \cdots L_n/2$, then (28) can be rewritten as

$$\sigma(l_n,\rho_{np}) = \sum_{k=-N_k(\eta_{nc})/2}^{N_k(\eta_{nc})/2} \sigma(\eta_{nc},\rho_{np},\theta_{nk}) \cdot \exp\left[j2\pi k W_{l_n}\right]. \tag{29}$$

$W_{l_n} = d_{l_n}\sin(\theta_{n0} - \beta_{l_n})/d_{L_n}$. d_{l_n}, β_{l_n} and d_{L_n} correspond to d_{η_n}, β_{η_n} and d_{T_n}, respectively. Compared with the formula of the NUFFT [27]-[28], we can find that (28) can be calculated by the NUFFT from the scattering coefficient $\sigma(\eta_{nc},\rho_{np},\theta_{nk})$ of the *k*-th subscene in the *p*-th equidistant ring domain at the subaperture central pulse position $A_{\eta_{nc}}$.

For the pulse l_n in the n-th subaperture, the equivalent scatterer's backscattering coefficient $\sigma(l_n,\rho_{np})$ of the p-th equidistant ring domain will be stored in the index l_n of $\sigma(\eta_{nc},\rho_{np},\theta_{nk})$ after NUFFT. It means that all the scattering coefficient $\sigma(l_n,\rho_{np})$ of the p-th equidistant ring for the n-th subaperture can be calculated by the NUFFT at the same time, which can improve the efficiency of the raw signal generation. Therefore, the scene's raw signal for the n-th subaperture can be computed by

$$s(\tau,\eta_n)\approx w_r(\tau)\exp(j\pi\gamma\tau^2)\otimes_\tau \sum_{p=1}^{N_p(\eta_{nc})}\left\{\mathrm{FFT}\left[\sigma(\eta_{nc},\rho_{np},\theta_{nk})\right]\cdot\exp\left[-j4\pi f_c\left(R(\eta_{nc},\rho_{np})+\Delta R_2\right)/c\right]\cdot\delta\left[\tau-2R(\eta_n,\rho_{np},\theta_{n0})/c\right]\right\} \quad (30)$$

3.3 Implementation

According to the principle of the proposed raw signal generation algorithm, its implementation is given as follows. Fig. 6 shows the flowchart of the implementation. Then, a brief description of the flowchart:

a. Set system simulation parameters and input the targets' backscattering coefficients of the scene.

b. Generate the transmitted signal and compute its FFT.

c. Divide the synthetic aperture into several subapertures.

d. Start subaperture processing, separate the scene into several equidistant ring domain and polar subscenes.

e. Calculate the equivalent scattering coefficient of polar subscenes at the subaperture center pulse. Then, based on the subscenes' scattering coefficient, calculate equidistant rings' scattering coefficient for all subaperture pulses by the NUFFT at the same time.

f. Calculate system's impulse response function and its FFT for all subaperture pulses.

g. Multiply the results of b and f, and then transform their product by IFFT to obtain subaperture pulses' echo signal.

h. In terms of subaperture order repeat (d)-(g) procedure, then the scene's echo signal can be generated.

4. Simulation Results

In order to verify the validity of the proposed method, simulation results are shown in this section. The raw signal generated by the TBT algorithm is used as the reference for the comparison, because this method has no approximation in theory. Besides, to further prove the correctness of the proposed algorithm by the evaluation of the imaging results, raw signals simulated by different methods are processed by backprojection algorithm (BPA), since it is the most accurate imaging algorithm. Here, SAR raw signals of the discrete scattering targets and nature scene are simulated.

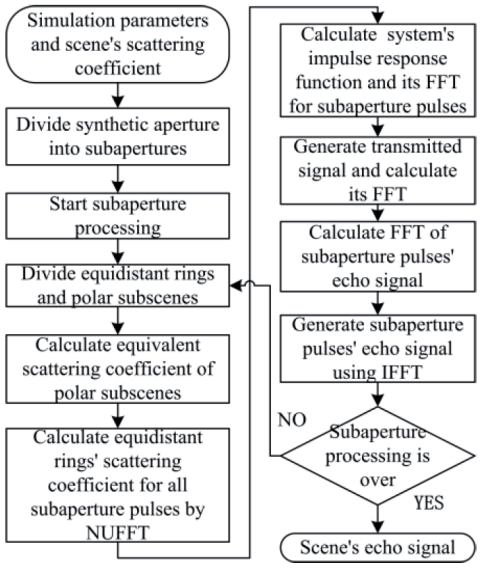

Fig. 6. Flowchart of the implementation of proposed method.

4.1 Discrete Scattering Targets Simulation

The simulation parameters are shown in Tab. 1. Based on the simulation parameters, it is easy to compute that the synthetic aperture time T_a is about 3.8 s. The motion errors are added to the nominal track of the radar. The azimuth error in Y axis is $\delta y=2\cdot\sin\left(2\pi\cdot(0.3/T_a)\eta\right)$, the range error in X axis is $\delta x=5\cdot\sin\left(2\pi\cdot(1/T_a)\eta\right)+0.3\eta$, and the altitude error in Z axis is $\delta z=3\cdot\sin\left(2\pi\cdot(0.5/T_a)\eta\right)$. 81 discrete scattering targets are located in scene, which are arranged in 9 rows and 9 columns. Range and azimuth spacing between the targets are 20.98 m and 22.44 m (in ground plane), respectively. The center scattering target's position is (1100 m, 0 m, 0 m). The backscattering coefficient of all scattering targets is assumed to be 1. Note that the jamming, thermal noise and clutter aren't considered in simulation.

Fig. 7 shows the simulated raw signals by the TBT and proposed algorithms. We can find that both amplitude and phase of the two raw signals look quite like each other. The amplitude relative error and phase error between two raw signals are given in Fig. 8, which is shown that the maximum amplitude relative error between two raw signals

Center frequency	400 MHz
Signal bandwidth	230 MHz
Sampling frequency	250 MHz
Pulse duration	1 μs
Pulse repetition frequency	100 Hz
Azimuth beamwidth	9.5°
Radar's nominal altitude	100 m
Radar's nominal velocity	45 m/s
Size of the scene	200 m × 200 m (range×azimuth)
Ground range of the scene centre	1100 m

Tab. 1. Simulation parameters for discrete scattering targets.

caused by the approximation of the equivalent scatterer and subaperture processing is about 0.01. The maximum phase error between two raw signals is about 0.201 radian, and its mean value and standard deviation are -4.079×10^{-7} radian and 0.0147 radian, respectively. These results prove the raw signal generated by the proposed method is precise.

To further verify the validity of the proposed method, raw signals generated by different methods are processed by the BPA, and the imaging results are shown in Fig. 9. From Fig. 9 (a) and (b), it is seen that all discrete scattering targets are full focused. Fig. 9 (c) and (d) show contours of the center target in the range [-30, 0] dB with a contour step of -3 dB, which are extracted from Fig. 9 (a) and (b), respectively. It is seen that the imaging result of the center target in Fig. 9 (d) is very close to that in Fig. 9 (c), but its focusing quality is slightly degraded due to approximations in raw signal generation. However, the effect is invisible at the high contour levels and some small influences can be observed at the lower contour levels.

The amplitude and phase profiles in the azimuth and range directions are shown in Fig. 10. From these figures, we can see clearly that both amplitude and phase profiles are almost identical. In the mainlobes of the amplitude profiles, it is impossible to see any difference between them. Whereas in the sidelobes of the amplitude profiles, there are slight differences between them. The similar performance can also be observed in the phase profiles, both in the range and azimuth directions.

The center target's resolution and PSLR are measured utilizing the amplitude profiles. The measured results are shown in Tab. 2. From Tab. 2, it is found that the measured parameters of the center target obtained from different raw signals are almost identical, and nearly theoretical results are achieved, which indicates that the presented raw signal generation algorithm is valid.

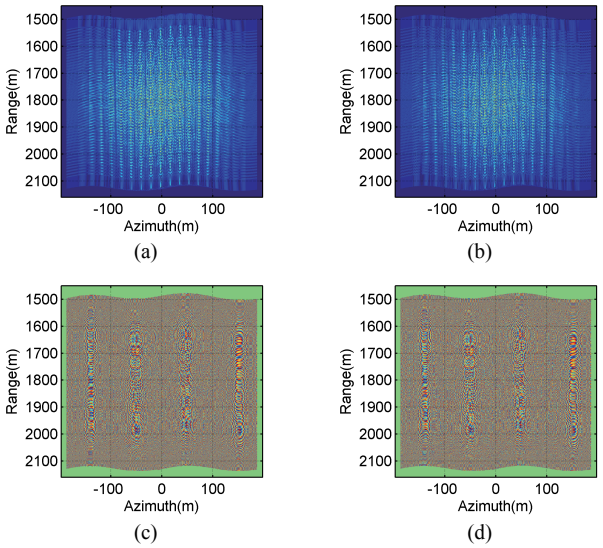

Fig. 7. Simulated raw signals of the discrete scattering targets. (a), (b) Amplitude and phase of the raw signal by the TBT algorithm; (c), (d) Amplitude and phase of the raw signal by the proposed algorithm.

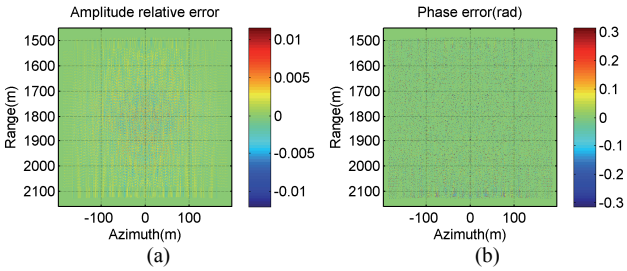

Fig. 8. Comparison between the simulated raw signals by different algorithms. (a) Amplitude relative error; (b) Phase error.

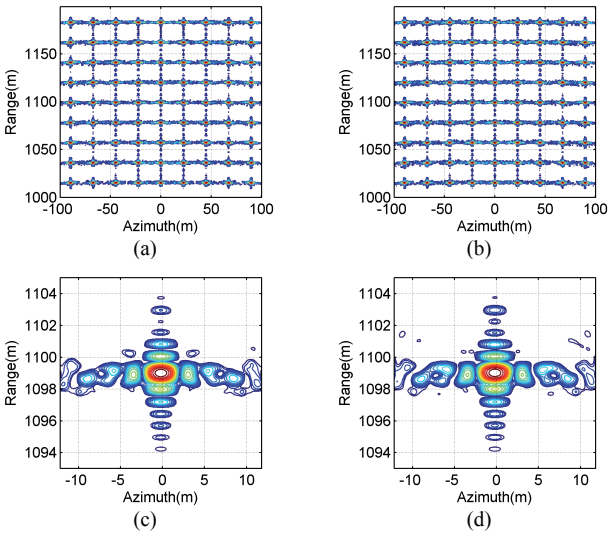

Fig. 9. Imaging results of the raw signals processed by the BPA. (a) TBT algorithm; (b) Proposed algorithm; (c) Imaging result of the center target in (a); (d) Imaging result of the center target in (b).

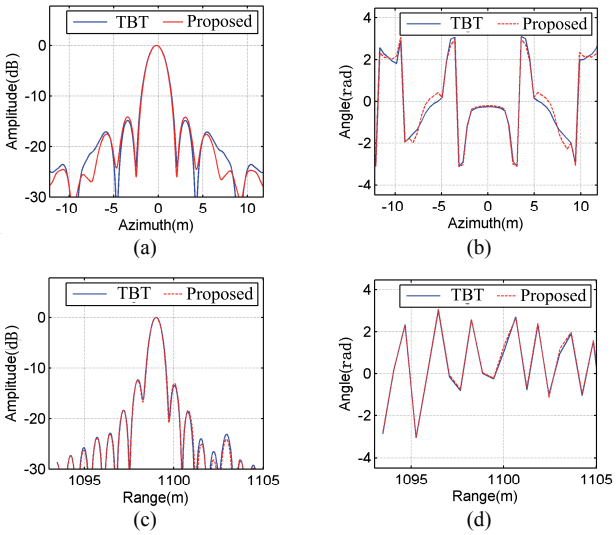

Fig. 10. Comparison between the results in Fig. 9(c) and (d). (a) Azimuth amplitude; (b) Azimuth phase; (c) Range amplitude; (d) Range phase.

To prove the simulation efficiency of the proposed method, the processing time of two algorithms is measured

on the same simulation condition. The two algorithms have been implemented in Matlab version 7.10.0 and on a computer with a 2.93 GHz Dual-Core processor and 2.00 GB RAM. Processing time of the TBT and proposed methods are 2243 s and 312.1 s, respectively. Compared with the TBT algorithm, the simulation efficiency of the proposed algorithm is improved about 7.18 times.

Measured parameters of the center target		Raw signal obtained by TBT method	Raw signal obtained by proposed method
Resolution	Azimuth	1.9575 m	1.9993 m
	Range	0.6415 m	0.6437 m
PSLR	Azimuth	13.47 dB	13.85 dB
	Range	13.35 dB	13.54 dB

Tab. 2. Measured parameters for the center target in the scene.

4.2 Nature Scene Raw Signal Simulation

To prove the feasibility of the proposed algorithm, the raw signal generation of the natural scene is performed.

The system simulation parameters for the natural scene are shown in Tab. 3. Fig. 11 is a high-resolution airborne SAR image with 1051 × 900 pixels. According to the point scattering model, single look complex data of the airborne SAR image can be directly regarded as the natural scene target's backscattering coefficient. And, TBT and proposed algorithms are used to simulate the natural scene's raw signal, which are also reconstructed by the BPA.

The simulated raw signals of the natural scene by the different methods are shown in Fig. 12. Fig. 13 gives the amplitude relative error and phase error between two raw signals in Fig. 12. It can be seen that two raw signals are very similar, and both amplitude relative error and phase error are very small, so the proposed method can satisfy the precise scene raw signal generation.

Fig. 14 shows the imaging results from the simulated raw signals in Fig. 12 by BPA, we can find that the nature scenes are reconstructed well. From the angle of sight, the simulated SAR images in Fig. 12 are similar to the real airborne SAR image in Fig. 11, and the only difference is that the former's resolution is lower than that of the latter. The reason is that the resolution scheduled in the simulated system is lower than that of the airborne SAR image, and the effects of the jamming, noise, clutter, multipath and incidence angle on target's backscattering coefficient aren't considered in simulation. The contours and the amplitude and phase profiles of the focused point target in the red rings in Fig. 14 are given in Fig. 15 and Fig. 16. We can find that the selected target is well focused, the focusing performance of the two imaging results are almost identical. Besides, the measured resolutions of this target are about 1.24 m in azimuth and 1.5 m in range, respectively.

Finally, the running time of the proposed algorithm is 1547.5 s comprised with the TBT method with 11204 s, which is acceptable for the scene simulation experiment.

Center frequency	400 MHz
Signal bandwidth	100 MHz
Sampling frequency	120 MHz
Pulse duration	1 μs
Pulse repetition frequency	100 Hz
Azimuth beamwidth	15.4°
Radar's nominal altitude	100 m
Radar's nominal velocity	45 m/s
Size of the scene	120 m × 195 m (range×azimuth)
Ground range of the scene centre	1060 m

Tab. 3. Simulation parameters for the natural scene.

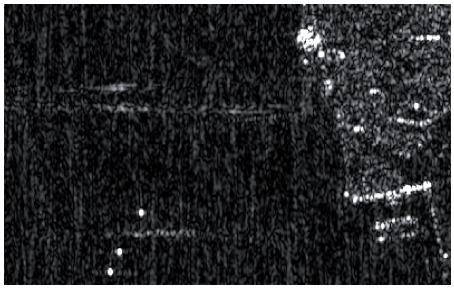

Fig. 11. Real airborne SAR image.

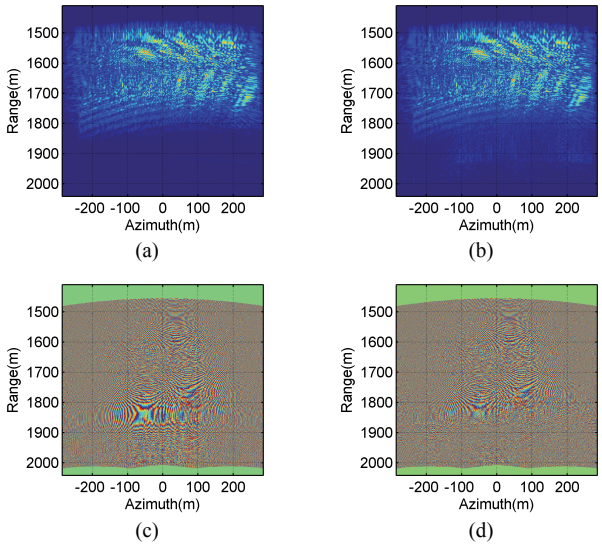

Fig. 12. Simulated raw signals of the natural scene. (a), (b) Amplitude and phase of the raw signal by the TBT algorithm; (c), (d) Amplitude and phase of the raw signal by the proposed algorithm.

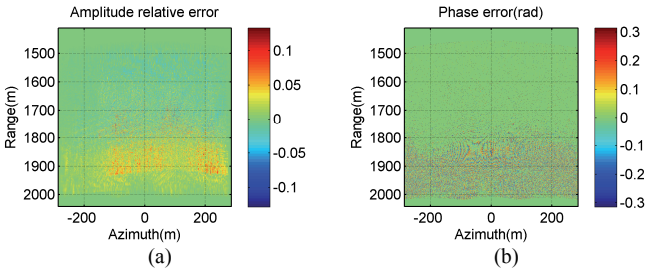

Fig. 13. Comparison between the simulated raw signals by different algorithms. (a) Amplitude relative error; (b) Phase error.

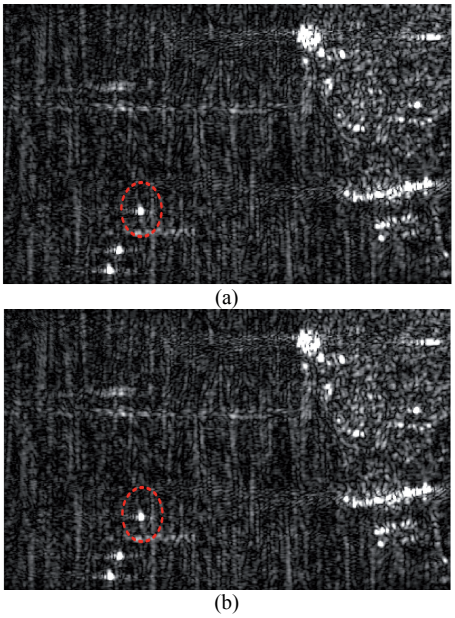

Fig. 14. Imaging results of the raw signals by the BPA. (a) TBT algorithm; (b) Proposed algorithm.

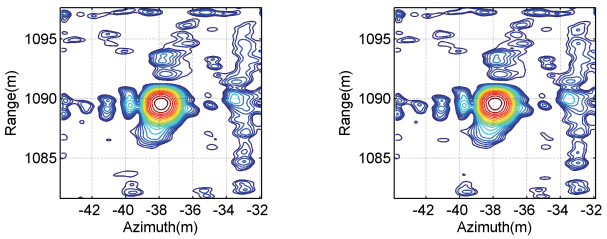

Fig. 15. Imaging results of the point target in the red rings in Fig. 14: (a) TBT algorithm; (b) Proposed algorithm.

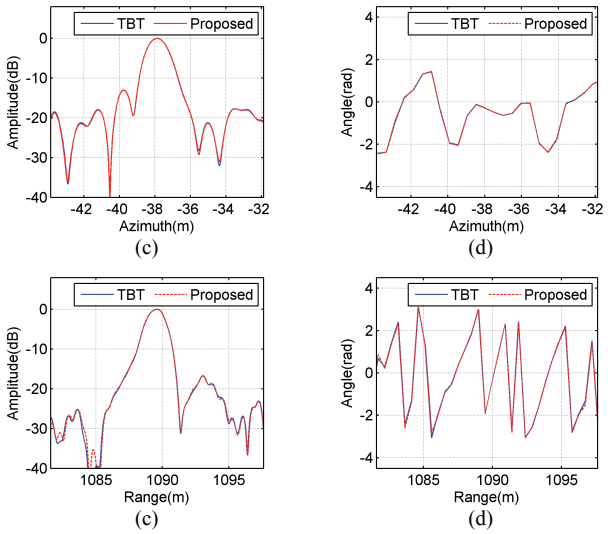

Fig. 16. Comparison between the imaging results in Fig.15. (a) Azimuth amplitude; (b) Azimuth phase; (c) Range amplitude; (d) Range phase.

In conclusion, the proposed raw signal generation method has high simulation precision and efficiency.

5. Conclusion

In the paper, a fast SAR raw signal generation method based on equivalent scatterer and subaperture processing is proposed. In this method, the subaperture processing and NUFFT are used to calculate the SAR system transfer function for the same subaperture pulses, then subaperture pulses' raw signal is generated by the convolution of the transmitted signal and system transfer function using FFT. It considers the radar's motion track to generate the precise raw signal for the real SAR. The utilization of the equivalent scatterer, subaperture processing and FFT (NUFFT) operation can greatly improve the efficiency of the SAR raw signal generation. The proposed method is verified by the simulation results, which has enriched and developed the SAR raw signal generation method.

However, to calculate the scattering coefficient of the equivalent scatterer for the same subaperture, the slant range approximation is used in the proposed simulation algorithm. Thus, it is needed to analyze the effect of the approximation error on the raw signal generation and imaging processing in the future research. In addition, with regard to the natural scene simulation, the complex data of the airborne SAR image is directly used as the target's backscattering coefficient. Thus, to generate more precise raw signal, the model and simulation of the nature scene should be investigated in the future research.

Acknowledgements

This work was supported by the National Natural Science Foundation of China under grant 61201329.

References

[1] CUMMING, I. G., WONG, F. H. *Digital Processing of Synthetic Aperture Radar Data: Algorithms and Implementation*. 1st ed. Norwood: Artech House, 2005.

[2] XIE, H., AN, D., HUANG, X., LI, X., ZHOU, Z. Fast factorised backprojection algorithm in elliptical polar coordinate for one-stationary bistatic very high frequency/ultrahigh frequency ultra wideband synthetic aperture radar with arbitrary motion. *IET Radar, Sonar and Navigation*, 2014, vol. 8, no. 8, p. 946–956, DOI: 10.1049/iet-rsn.2012.0350.

[3] XIE, H., AN, D., HUANG, X., ZHOU, Z. Fast time-domain imaging in elliptical polar coordinate for general bistatic VHF/UHF ultra-wideband SAR with arbitrary motion. *IEEE Journal of Selected Topics in Applied Earth Observations and Remote Sensing*, September 2014, DOI: 10.1109/JSTARS.2014.2347413.

[4] FRANCESCHETTI, G., MIGLIACCIO, M., RICCIO, D., SCHIRINZI, G. SARAS: A synthetic aperture radar (SAR) raw signal simulator. *IEEE Transactions on Geoscience and Remote Sensing*, 1992, vol. 30, no. 1, p. 110–123.

[5] CIMMINO, S., FRANCESCHETTI, G., IODICE, A., RICCIO, D., RUELLO, G. Efficient spotlight SAR raw signal simulation of

extended scenes. *IEEE Transactions on Geoscience and Remote Sensing*, 2003, vol. 41, no. 10, p. 2329–2337.

[6] QIU, X., HU, D., ZHOU, L., DING, C. A bistatic SAR raw data simulator based on inverse ω-k algorithm. *IEEE Transactions on Geoscience and Remote Sensing*, 2010, vol. 48, no. 3, p. 1540 to 1547.

[7] LIN, Y. C., SARABANDI, K. A Monte Carlo coherent scattering model for forest canopies using fractal-generated trees. *IEEE Transactions on Geoscience and Remote Sensing*, 1999, vol. 37, no. 1, p. 440–451.

[8] BROWN, C. G., SARABANDI, K., GILGENBACH, M. Physics-based simulation of high-resolution polarimetric SAR images of forested areas. In *Proceedings of IEEE International Geoscience and Remote Sensing Symposium*. Toronto (Canada), 2002, p. 466 to 468.

[9] FRANCESCHETTI, G., MIGLIACCIO, M., RICCIO, D. On ocean SAR raw signal simulation. *IEEE Transactions on Geoscience and Remote Sensing*, 1998, vol. 38, no. 1, p. 84–100.

[10] FRANCESCHETTI, G., IODICE, A., RICCIO, D. A canonical problem in electromagnetic backscattering from buildings. *IEEE Transactions on Geoscience and Remote Sensing*, 2002, vol. 40, no. 8, p. 1787–1801.

[11] FRANCESCHETTI, G., IODICE, A., RICCIO, D., RUELLO, G. SAR raw signal simulation for urban structures. *IEEE Transactions on Geoscience and Remote Sensing*, 2003, vol. 41, no. 9, p. 1986–1995.

[12] WANG, Z. L., XU, F., JIN, Y. Q., OGURA, H. A double Kirchhoff approximation for very rough surface scattering using the stochastic functional approach. *Radio Sci*ence, 2005, vol. 40, no. 4, RS4011, DOI: 10.1029/2004RS003079.

[13] XU, F., JIN, Y. Q. Deorientation theory of polarimetric scattering targets and application to terrain surface classification. *IEEE Transactions on Geoscience and Remote Sensing*, 2005, vol. 43, no. 10, p. 2351–2364.

[14] XU, F., JIN, Y. Q. Imaging simulation of polarimetric synthetic aperture radar for comprehensive terrain scene using the mapping and projection algorithm. *IEEE Transactions on Geoscience and Remote Sensing*, 2006, vol. 44, no. 11, p. 3219–3234.

[15] YONGYAN, L. *SAR Image*. Harbin: Harbin Institute of Technology Press, 1999.

[16] FRANCESCHETTI, G., IODICE, A., RICCIO, D., RUELLO, G. A 2-D Fourier domain approach for spotlight SAR raw signal simulation of extended scenes. In *Proceedings of IEEE International Geoscience and Remote Sensing Symposium*. Toronto (Canada), 2002, p. 853–855.

[17] FRANCESCHETTI, G., IODICE, A., PERNA, S., RICCIO, D. Efficient simulation of airborne SAR raw data of extended scenes *IEEE Transactions on Geoscience and Remote Sensing*, 2006, vol. 44, no. 10, p. 2851–860.

[18] FRANCESCHETTI, G., IODICE, A., PERNA, S., RICCIO, D. SAR sensor trajectory deviations: Fourier domain formulation and extended scene simulation of raw signal. *IEEE Transactions on Geoscience and Remote Sensing*, 2006, vol. 44, no. 9, p. 2323 to 2334.

[19] FRANCESCHETTI, G., GUIDA, R., IODICE, A., RICCIO, D., RUELLO, G., STILLA, U. Simulation tools for interpretation of high resolution SAR images of urban areas. In *Proceedings of Urban Remote Sensing Joint Event*. Paris (France), 2007, p. 1–5.

[20] WANG, Y., ZHANG, Z., DENG, Y. Squint spotlight SAR raw signal simulation in the frequency domain using optical principles. *IEEE Transactions on Geoscience and Remote Sensing*, 2008, vol. 46, no. 8, p. 2208–2215.

[21] KHWAJA, A. S., FERRO-FAMIL, L., POTTIER, E. SAR raw data simulation using high precision focusing methods. In *Proceedings of European Radar Conference*. Paris (France), 2005, p. 33–36.

[22] KHWAJA, A. S., FERRO-FAMIL, L., POTTIER, E. Efficient SAR raw data generation for anisotropic urban scenes based on inverse processing. *IEEE Geoscience and Remote Sensing Letters*, 2009, vol. 6, no. 4, p. 757–761.

[23] HUANG, L., WANG, Z., ZHENG, T. A fast algorithm based on FFT used in simulation of SAR return wave signal. *Journal of Remote Sensing*, 2004, vol. 8, no. 2, p. 128–136.

[24] ZHANG, S., LONG, T., AENG, T., DING, Z. Space-borne synthetic aperture radar received data simulation based on airborne SAR image data. *Advances in Space Research*, 2008, vol. 41, no. 11, p. 181–182.

[25] WEN, L., ZHENG, T. A sub-aperture based SAR raw signal generation method. In *Proceedings of IET International Radar Conference*. Guilin (China), 2009, p. 89–92.

[26] ZHANG, S., ZHANG, W., KONG, L. SAR raw signal simulation based on sub-aperture processing. In *Proceedings of International Radar Conference*. Washington (USA), 2010, p. 569–572.

[27] LIU, Q. H., NGUYEN, N. An accurate algorithm for nonuniform fast Fourier transforms (NUFFT's). *IEEE Microwave and Guided Wave Letters*, 1998, vol. 8, no. 1, p. 18–20.

[28] ANDERSSON, F., MOSES, R., NATTERER, F. Fast Fourier methods for synthetic aperture radar imaging. *IEEE Transactions on Aerospace and Electronic Systems*, 2012, vol. 48, no. 1, p. 215 to 229.

About Authors …

Hongtu XIE was born in Hunan, China. He received his B.Sc. from the Hunan University in 2008 and his M.Sc. from the National University of Defense Technology (NUDT) in 2010. His research interests include the low frequency ultra wideband (UWB) SAR imaging.

Daoxiang AN was born in Jilin, China. He received his B.Sc., M.Sc. and Ph.D. from the National University of Defense Technology in 2004, 2006 and 2011, respectively. He is currently a Lecturer with the NUDT. His research interests include the UWB SAR imaging.

Xiaotao HUANG was born in Hubei, China. He received his B.Sc. and Ph.D. from the National University of Defense Technology in 1990 and 1999, respectively. He is currently a Professor with the NUDT. His research interests include the radar theory and signal processing.

Zhimin ZHOU was born in Hebei, China. He received the B.Sc., M.Sc. and Ph.D. from the National University of Defense Technology in 1982, 1989, and 2002, respectively. He is currently a Professor with the NUDT. His research interest includes UWB radar system and signal processing.